Scattering effects from neighboring atoms in core-level WSe_2 photoemission

M. J. Ambrosio,[1] E. Plésiat,[2] P. Decleva,[3] P. M. Echenique,[1,4] R. Díez Muiño,[1,5] and F. Martín[2,6]

[1]*Donostia International Physics Center, 20018 San Sebastián, Spain*

[2]*Instituto Madrileño de Estudios Avanzados de Nanociencia, Campus de Cantoblanco, 28049 Madrid, Spain*

[3]*Dipartamento di Scienze Chimiche e Farmaceutiche, Universitá di Trieste, 34127 Trieste, Italy*

[4]*Universidad del País Vasco, Apdo. 1072, 20018 San Sebastián, Spain*

[5]*Centro de Física de Materiales (CSIC/UPV-EHU), 20018 San Sebastián, Spain*

[6]*Departamento de Química, Universidad Autónoma de Madrid, 28049 Madrid, Spain*

(Received 17 November 2021; revised 31 January 2022; accepted 10 February 2022; published 8 March 2022)

Methods of attosecond science originally developed to investigate systems in the gas phase are currently being adapted to obtain temporal information on the electron dynamics that takes place in condensed-matter systems. In particular, streaking measurements have recently been performed to determine photoemission time delays from the WSe_2 dichalcogenide. In this work we present a fully atomistic description of the photoemission process in WSe_2 and provide angularly resolved photoemission cross sections and time delays from the W $4f$, Se $3d$ and Se $4s$ core states of the system. Since these states are spatially localized, we propose a cluster approach in which we build up from smaller to larger clusters, so that we can assess the importance of scattering effects by each new layer of neighboring atoms. We use a static-exchange density functional theory method with B-spline functions, where a one-center angular-momentum expansion is supplemented by off-center expansions with fewer partial waves. This enhances convergence in comparison with a one-center expansion, which would require very high angular momenta to characterize the localized fast oscillations near each off-center atomic core. We find that the photoemission delays and fully differential cross sections are strongly affected by scattering events that take place off the neighboring atoms, implying the need to consider their effects for quantitative descriptions of the photoemission process.

DOI: 10.1103/PhysRevB.105.125405

I. INTRODUCTION

Transition metal dichalcogenides (TMDCs) are a family of two-dimensional materials, whose composition follows the formula MX_2, with M a group IV, V, or VI transition metal while X denotes a chalcogen, examples of which are S, Se, and Te. WSe_2 belongs to the TMDC family and is a semiconductor, which can be both, n- and p-doped, making it suitable for electronic devices requiring p-n junctions. Internally, each $2H$-WSe_2 layer is held together by covalent-ionic bonds between a W atom and the six closest Se atoms. Relatively weak van der Waals bonds between layers mean that few- or single-layer structures can be produced by an exfoliation process [1]. Its most stable form is the $2H$ structure, an A-B-A-B stacking [2], the B layers having an in-plane reflection with respect to A layers. Other less common or stable forms for TMDCs, which have different interlayer displacements and coordinations, are $3R$, $1T$, and $1T'$ [3].

In its bulk form, WSe_2 possesses an indirect band gap (1.25 eV), which becomes direct and wider (1.9 eV) reaching the monolayer configuration, making it favorable for photonic applications [4]. Band structure [2] and dielectric function tuning can be achieved by mechanical strain, which results in varying electrical and optical properties [5–7]. Doping and defects are also means of modifying the TMDC's characteristics [1]. A review on the possible applications of WSe_2 in the field of electronics, photoelectronics, and gas sensors can be found in [1].

The high potential of WSe_2 for applications has drawn recent interest towards a better understanding of the electron-substrate and light-electron interactions via angle-resolved photoelectron spectroscopy (ARPES) or time- and angle-resolved photoelectron spectroscopy (TRARPES). Tanabe *et al.* [8] probed the symmetries of the valence band states using ARPES, while in a recent application of TRARPES by Liu *et al.* [9], the authors apply a 28 eV probe and a 1.55 eV pump pulse to excite electrons from the valence band. Taking advantage of the spatial localization of core states, in comparison with the delocalized nature of the valence-band states probed in the above-mentioned experiments, TRARPES has also been used to get insight into the photoemission time delays from the deeply bound W $4f$, Se $3d$, and Se $4s$ states of WSe_2 [10]. In this experiment, attosecond-streaked spectra from the core states were measured and, using the streaking traces from the Se $4s$ state as a reference, relative photoemission time delays were determined.

Attosecond streaking generates a spectrum that can be understood from a classical picture, where the electron is alternatively slowed down and sped up by an IR dressing field after being promoted to the continuum by an XUV pulse. The measured delays thus contain dynamical information of the escaping photoelectron from its birth to its final destination

outside the material. Hence, in addition to the initial state characteristics (e.g., the initial angular momentum), the rich dynamics that the photoelectron undergoes on its way to the continuum is also imprinted in the measured signal. Due to the inherent complexity of a periodic solid system such as WSe_2, previous quantum mechanical models separate the contribution of the different effects and do not describe the surrounding atoms on the same footing as the atoms from which the electron is ejected [10]. Purely classical Monte Carlo calculations can more easily handle the latter effect and, in fact, have been successfully used to characterize the physics of the escaping electron in metal nanoparticles [11,12], but logically they are not fully appropriate when quantum interferences are expected to play a prominent role. Thus, a full quantum mechanical treatment that treats all atomic centers at a similar level of accuracy and describes the expected interferences between different electronic paths associated with multiple scattering events is highly desirable to better understand the physics of the photoemission process in TMDCs.

In this work we present a fully atomistic quantum mechanical description of the photoemission process in WSe_2 and provide angularly resolved photoemission cross sections and time delays from the W $4f$, Se $3d$, and Se $4s$ core states of the system. Since these states are spatially localized, we propose a cluster approach in which we build up from smaller to larger clusters, so that we can assess the importance of scattering effects by each new layer of neighboring atoms. Our method consists of a static-exchange density functional theory (DFT) partial-wave expansion with supplemental off-center terms. The radial coordinates are discretized by sets of B-spline functions. The method has a proven track record when applied to single-photon electron spectroscopy from small molecules [13–16], while more recently it has been extended to time-resolved spectroscopy [17]. In this contribution we are extending the method to the realm of solid state physics. We show that the photoemission delays and fully differential cross sections are strongly affected by scattering events that take place off the neighboring atoms, implying the need to consider such effects for a quantitative description of the photoemission process.

The paper is organized as follows. First we present the necessary theory for our model, then we examine how the fully differential cross section evolves for increasingly larger clusters, assessing whether convergence is achieved with respect to the cluster size, and then we focus on a more detailed cross-section-and-Wigner-delay joint analysis. This more detailed study is performed mainly for the few-atom clusters, where the nature of the photoelectron interactions with the cluster can be inferred. We start the analysis by the small clusters, namely, Se2, W_3Se, W_3Se_2, WSe_3, and WSe_6, and use the acquired information to tackle the more complex clusters: W_7Se_6, W_7Se_{12}, W_7Se_{24}, W_3Se_{14}, and W_6Se_{14}. All clusters are depicted in Fig. 1.

II. THEORY

The objective of this work is to evaluate transition amplitudes, and from them, extract the physically measurable fully differential cross sections (FDCS) and Wigner time

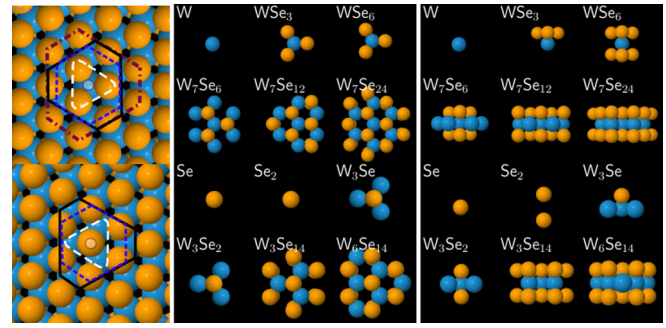

FIG. 1. Top left panel: Diagram indicating the W-centric model clusters within the periodic crystal. WSe_3: white long-dashed line. W_7Se_6: blue short-dashed line. W_7Se_{12}: black solid line. W_7Se_{24}: maroon dot-dashed line. Bottom left panel: Se-centric model clusters. W_3Se W_3Se_2: white long-dashed line. W_3Se_{14}: blue short-dashed line. W_6Se_{14}: black solid line. Center column: top view of every model cluster in this work. Right column: side view of every model cluster in this work.

delays for WSe_2 one-photon ionization. Our technique incorporates effects introduced by the neighboring atoms into the photoemission process as in state-of-the-art theoretical studies of molecular photoionization. In order to calculate transition-matrix elements we first obtain the initial and final (continuum) states for the system in question by diagonalizing the Kohn-Sham Hamiltonian

$$H_{KS} = -\frac{1}{2}\nabla^2 - \sum_N \frac{Z_N}{|\boldsymbol{r} - \boldsymbol{R}_N|} + \int \frac{n(\boldsymbol{r}')}{|\boldsymbol{r} - \boldsymbol{r}'|} + V_{XC}[n(\boldsymbol{r})], \tag{1}$$

where V_{XC} is the LB94 exchange-correlation functional [18], $\boldsymbol{R}_N$ are the nuclei positions, and Z_N their charges. The LB94 functional has been chosen to guarantee that the photoelectron sees the correct asymptotic charge in its escape from the atomic center. The ground state density $n(\mathbf{r}')$ has been evaluated with the Amsterdam density functional (ADF) commercial software [19–22]. Bound states, with negative eigenvalues, are directly provided by diagonalization of the Kohn-Sham Hamiltonian in Eq. (1), while continuum asymptotic-momentum eigenstates at a chosen positive energy are obtained by solving the scattering K-matrix equations in the basis of KS orbitals through an inverse iteration procedure [13,15,23]. This procedure, which is widely used to describe the electronic continuum of atoms and molecules in the gas phase, ensures that the correct asymptotic boundary conditions of scattering states are correctly imposed. Continuum states have been evaluated for energies between 0 and 110 eV, with particular attention to 91 eV, which is the energy chosen in Ref. [10] for their streaking measurements.

The wave functions are represented in a basis of B-spline functions located at the center of mass of the cluster [one-center expansion (OCE)] for different symmetry-adapted partial waves, complemented by smaller off-center angular-momentum expansions located at the nuclei's positions. We adopt a notation similar to Toffoli *et al.* [15], and denote the OCE basis elements at the origin O by

$$\chi^O_{nlh\lambda\mu} = \frac{1}{r_O} B_n(r_O) X_{lh\lambda\mu}(\theta_O, \phi_O), \tag{2}$$

TABLE I. One-center angular momentum L_{MAX}: semiclassical estimate and the values used in this report to ensure convergence.

W-centric	W	WSe_3	WSe_6	W_7Se_6	W_7Se_{12}	W_7Se_{24}
Semiclassical		12	12	16	20	25
Converged	10	24	24	26	32	40
Se-centric	Se	Se2	W_3Se	W_3Se_2	W_3Se_{14}	W_6Se_{14}
Semiclassical		8	9	9	18	19
Converged	10	24	20	26	28	28

and define the angular functions X as

$$X_{lh\lambda\mu}(\theta,\phi)=\sum_m Y^R_{lm}(\theta,\phi)\beta_{lmh\lambda\mu}, \tag{3}$$

with Y^R_{lm} being real spherical harmonics and the coefficients $\beta_{lmh\lambda\mu}$ give the symmetry-dictated weights. The off-center basis elements are symmetrized combinations of functions localized at each augmentation sphere j:

$$\chi^i_{nlh\lambda\mu}=\sum_{j\in Q_i}\frac{1}{r_j}B_n(r_j)\sum_m \beta^{(j)}_{lmh\lambda\mu}Y^R_{lm}(\theta_j,\phi_j). \tag{4}$$

Index i runs over the nonequivalent nuclei sets, denoted by Q_i, while j enumerates the equivalent centers within each Q_i. Each center has its set of off-center coordinates r_j,θ_j,ϕ_j. λ indicates the irreducible representation, while μ denotes the degeneracy, if present, and h identifies elements within a set fixed by l,λ,μ. Turning to the radial coordinates, B_n stands for the nth spline basis element. The B-spline bases span the radial interval $[0,R^Q_{\mathrm{MAX}}]$ for the main expansion, and $[0,R^i_{\mathrm{MAX}}]$ for the off-center ones. Indices l,m are the usual angular-momentum quantum numbers. For the off centers we chose a maximum angular momentum L^j_{MAX} one unit larger than the highest bound-state angular momentum, in order for the basis to properly describe continuum states accounting for dipole emission near each core. The B-spline basis set is truncated at the outermost radius by excluding the three outermost B splines from each off-center basis in order to achieve continuity up to the second derivative at $r_j=R^j_{\mathrm{MAX}}$. The B-spline knot grid is tuned to have a finer step near the cores, reaching an asymptotic value far away from the main center.

A simple semiclassical estimation provides a starting point, a baseline, for the main angular-momentum expansion. We calculate the classical angular momentum of an electron with maximum linear momentum placed at the farthest atomic core. This acts as a bare minimum of the angular momentum L_{MAX} of the main partial-wave expansion. Table I shows the bare minimum L_{MAX} by the semiclassical requirement for an asymptotic kinetic energy of 3 a.u., as well as the final values with which numerical convergence was reached.

In all cases the semiclassical baseline was indeed surpassed by the angular-momentum values that ensured convergence. A quantum mechanical interpretation surmises the minimum L_{MAX} requirement as related to the number of partial waves necessary to characterize the wave function oscillations in the transverse direction at the cluster's farthest atomic positions. The off-center complementary expansions, which take care of the very tightly localized oscillations at each atomic center, account for the expected increase in the kinetic energy of the electron due to the deep atomic-core potential wells.

We evaluate the photoemission transition matrix for $\boldsymbol{\epsilon}$-polarized light, starting from a bound (*initial, i*) molecular orbital (MO) Ψ^i_J indexed by J to a (*final, f*) $\mathbf{k}_f$-asymptotic-momentum state $\Psi^f_{\mathbf{k}_f}$ [24]:

$$T_{\mathbf{k}_f,J}=\left\langle\Psi^f_{\mathbf{k}_f}\middle|\boldsymbol{\epsilon}\cdot\mathbf{r}\middle|\Psi^i_J\right\rangle. \tag{5}$$

The fully differential cross section is subsequently derived [24], as

$$\frac{d\sigma_J}{d\Omega}=\frac{8\pi\omega|T_{\mathbf{k}_f,J}|^2}{3c}, \tag{6}$$

with c being the speed of light ($\approx$137 a.u.) and ω the photon energy. The Wigner photoemission delay is given by

$$\tau_{\mathrm{Wig}}=\frac{d\varphi_J}{dE_f}, \tag{7a}$$

$$\varphi_J=\arg(T_{\mathbf{k}_f,J}), \tag{7b}$$

i.e., the derivative of the transition-element phase with respect to the kinetic energy E_f (see Refs. [25–28]).

Emission from W $4f$ was modeled by considering clusters which had a central W atom, namely, WSe_3, WSe_6, W_7Se_6, W_7Se_{12}, and W_7Se_{24}. For Se $3d$ and Se $4s$ emission we chose arrays with one or two atoms at their central axis: Se_2, W_3Se, W_3Se_2, W_3Se_{14}, and W_6Se_{14}. Figure 1 (left panels) shows how the model clusters progressively incorporate neighboring atoms from the full periodic system.

Photoemission from localized cores, especially nonzero-angular-momentum orbitals, implies the aggregation of photoelectrons from a number of MOs. Specifically, we are interested in the emission from the central atoms, since they are the ones this cluster approach intends to model, by progressively surrounding them with additional neighbors. Due to the symmetry properties of the clusters, we find that, to a very good approximation, the probability density associated with all degenerate localized orbitals (LOs) coincides with that resulting from an incoherent sum over the MOs given in Table II. The information in this table has been obtained by observing the molecular orbital construction in terms of symmetry-adapted atomic orbitals after the ADF-calculation stage. An example of how to read the information in Table II is as follows: MOs $35A1'$, $22A2'$, $54E'$ (doubly degenerate), $21A2''$, and $31E''$ (doubly degenerate) are the mutually orthogonal W $4f$ LOs (i.e., $4f_{-3}$, $4f_{-2}$, $4f_{-1}$, $4f_0$, $4f_{+1}$, $4f_{+2}$, and $4f_{+3}$) of the central W atom in W_7Se_6. Therefore, to calculate the Wigner delay and cross section corresponding to the LO, we need to gather those indexes for the said MOs.

Following a recipe similar to that proposed in Ref. [29], we use the following cross-section-weighted average to evaluate the Wigner delay associated with all degenerate LOs:

$$\tilde{\tau}_{\mathrm{Wig},I}(\theta,\phi)=\frac{\sum_J\frac{d\sigma_J}{d\Omega}(\theta,\phi)\tau_{\mathrm{Wig},J}(\theta,\phi)}{\sum_J\frac{d\sigma_J}{d\Omega}(\theta,\phi)}, \tag{8}$$

where J indexes the MOs (e.g., $22A2'$), and I identifies the set of degenerate LOs (e.g., $4f_{-3}$, $4f_{-2}$, $4f_{-1}$, $4f_0$, $4f_{+1}$, $4f_{+2}$,

TABLE II. Localized orbitals (LO) composition in terms of molecular orbital (MO) of point groups C_{3v} or D_{3h}, indexed by growing principal quantum number within their subspecies $A1$, $A2$, E and $A1'$, $A2'$, E', $A1''$, $A2''$, E''.

	LO	$A1$	$A2$	E		
W $4f$ @ W	11,12	1	8,9			
Se $3d$ @ Se	6		3,4			
Se $4s$ @ Se	7					
LO	$A1'$	$A2'$	E'	$A1''$	$A2''$	E''
W $4f$ @ WSe_6	18	5	20		14	17
W $4f$ @ W_7Se_6	35	22	54		21	31
W $4f$ @ W_7Se_{12}	45	26	68		31	45
W $4f$ @ W_7Se_{24}	63	44	104		48	79
Se $3d$ @ W_3Se_2	18		20,21		11	10,11
Se $3d$ @ W_3Se_{14}	27		55,56		25	35,36
Se $3d$ @ W_6Se_{14}	39		38,39		20	28,29
Se $4s$ @ W_3Se_2	22				15	
Se $4s$ @ W_3Se_{14}	36				29	
Se $4s$ @ W_6Se_{14}	51				37	

and $4f_{+3}$ for W $4f$). The corresponding FDCS is just the incoherent sum of the FDCSs for each degenerate state.

The FDCS and Wigner delay $\tilde{\tau}_{\mathrm{Wig},I}$ in Eq. (8) are defined for each emission direction and energy. For finite collection angles we define an integrated Wigner time delay $\langle\tilde{\tau}_{\mathrm{Wig},I}\rangle$ as follows [29]:

$$\langle\tilde{\tau}_{\mathrm{Wig},I}\rangle = \frac{\int \frac{d\sigma}{d\Omega}(\theta,\phi)\tau_{\mathrm{Wig}}(\theta,\phi)d\Omega}{\int \frac{d\sigma}{d\Omega}(\theta,\phi)d\Omega}. \tag{9}$$

Our symmetry-adapted partial wave expansion makes use of point-group theory, leading to transition matrices for each molecular orbital. Since we are interested in the emission from the innermost atoms, as opposed to emission from the whole cluster, we need a way to separate the center-specific contributions. To that end we observe the symmetry-adapted orbital composition (symmetry combinations of fragment orbitals, or SFO in ADF [19]) in terms of individual-atom orbitals from ADF, and in turn how these SFOs are combined to create the molecular orbitals. As a by-product of point-group symmetry, the photoelectron yield from the core levels of interest is, to good approximation, made up of incoherent MO contributions. This is due to some of the MOs being completely localized by construction, meaning they are dominantly constituted by one ADF SFO which in turn is dominated by orbitals belonging to an innermost atom or atomic pair. Therefore, in order to obtain observables like the cross section or Wigner delay, we are able to combine the yields incoherently. As a consequence, the probability contribution from the central W $4f$ orbitals is to within 99% constructed as the incoherent summation of a specific MO's yield. The same applies for the Se $3d$ orbitals from the innermost Se atoms, to about 99%, and lowering for Se $4s$ to about 60%. Table II specifically shows which MOs the localized-orbital photocurrent stems from.

All the model clusters belong to either the C_{3v} or the D_{3h} point groups with the Se_2 and isolated atoms being the exceptions and belonging to higher-symmetry groups (C_∞ and R_3). This means that all the systems will present a minimum of three vertical symmetry planes.

III. RESULTS

We arrange the results as follows. In Sec. III A we show polar FDCS plots as a function of the emission directions for a fixed photon energy of 91 eV, as in the experiment [10], where the growing emission-pattern complexity becomes evident as we consider bigger model clusters. Section III C explores the scattering mechanisms that emerge with the gradual addition of atoms to the clusters, outlining the processes that lead to observable cross section and Wigner delay structures. We stress that this procedure relies on comparing calculations for progressively larger clusters, in order to disentangle the information by comparison. The convergence with respect to cluster size is addressed in Sec. IV.

A. Fully differential cross section

Based on the experimental conditions from Ref. [10], we consider a photon energy of 91 eV and we present the detailed FDCS structure with respect to the outgoing direction in Figs. 2–4.

The addition of neighbor-atom layers plays a role in the FDCS shape more significantly than initially expected. Given that the core levels are strongly localized, we expect the effects to stem from the final state, which contains every possible scattering and confinement process. Figures 2(a) and 2(h) show that the presence of the top Se layer draws the photoemission from the central W atom, deflecting it in the direction of the Se cores. Panel (c) incorporates the bottom three-Se-atom layer. Besides the three-lobed emission being tilted towards the Se atoms, each lobe is distorted, presenting small shoulder structures, which are due to a reflection effect. This will become more apparent when we jointly analyze the FDCSs and Wigner delays in Sec. III C. A subsequent incorporation of a W ring seems to focus the lobes towards normal emission, as shown in panels (d) and (j). The addition of an outer perimeter of Se atoms [see panels (e) and (k) in Fig. 2] introduces higher complexity in the FDCS. The simple three-lobe upwards and downwards structures give way to a number of fine protrusions but also a focused normal-emission

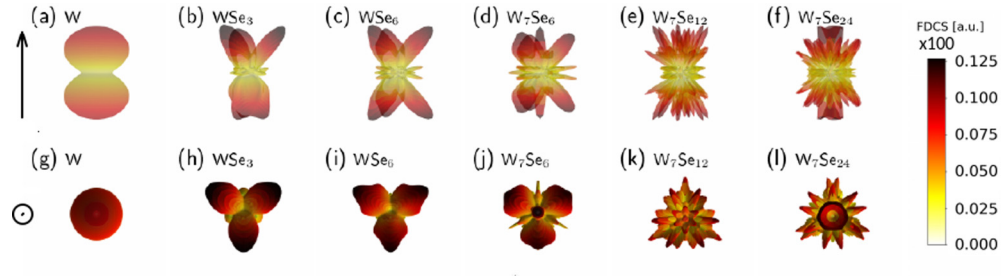

FIG. 2. Top row: Side view of the W $4f$ photoemission FDCS at 91 eV photon energy, with light polarization along the z axis (indicated by the leftmost arrow and circle). Bottom row: top view of the W $4f$ FDCS.

peak [see panels (e), (f), (k), and (l) from Fig. 2]. When comparing with the results of larger clusters, W_7Se_{24} to W_7Se_{12}, we observe that the W $4f$ FDCS has not reached complete convergence. At the same time, the comparison shows that the effects are mostly rounding up the existing shape, in addition to an upward-focusing effect. From a purely mathematical perspective, the addition of more atomic perimeters introduces higher angular-momentum partial waves, which translates into higher L_{MAX} needed to achieve numerical convergence. In turn, higher angular momenta enables the finer photoemission lobes [cf. left to right halves in Figs. 2, 3, and 4].

We now turn to Se-centric systems, namely, Se, Se_2, W_3Se, W_3Se_2, W_3Se_{14}, and W_6Se_{14}. The study evidences a better cluster-size converged picture. We start with the Se $3d$ state, building up from the isolated atom. The addition of a second Se atom as emitter creates interference, as attested by the middle rings in the FDCS, and increases the photoelectron yield [cf. Fig. 3, panels (a) and (b)]. The yield increase is, as expected, present in the comparison between W_3Se and W_3Se_2; however, these systems incorporate the threefold vertical symmetry. Turning to the more sophisticated clusters in panels (e) and (f) [and (k) and (l)] we see that the FDCS exhibits only minor changes while keeping the overall pattern in place. The cluster model for Se $3d$ emission shows a better degree of convergence than the models for W $4f$.

The scenario for the Se $4s$ photoemission (see Fig. 4) is much more simplistic than for the Se $3d$ and W $4f$ orbitals. The dipole nature of the s-type-orbital photoemission shape dominates all the cases but W_3Se. We observe that the cluster produces a focusing effect towards normal emission at photon energies near 91 eV, with only a minor flux scattered away from the z axis. The FDCS shape largely stabilizes even with a relatively small cluster, W_3Se_2, varying by less than a factor 2 towards W_3Se_{14} and W_6Se_{14}. The shape change between W_3Se_{14} to W_6Se_{14} is a minor off-axis lobe narrowing.

B. Wigner delays

Here, we present the Wigner time delays resulting from each cluster model for each of the orbitals of interest. The Wigner delays correspond solely to the ionization process induced by XUV radiation [30], and they—-or their differences between selected orbitals—are not expected to match the values obtained from streaking measurements, which are affected by the so-called continuum-continuum delays introduced by the accompanying IR pulse. The experimental measurement from Siek *et al.* [10] collected photoelectrons emitted perpendicular to the surface, therefore we adjust the collection angle around the normal axis, setting the collection width to 5°. Table III shows the calculated Wigner delays in this angular range.

While for W emission the Wigner delay $\langle \tilde{\tau}_{\mathrm{Wig},I} \rangle$ shows appreciable changes even for the largest clusters, the opposite is true for both Se $3d$ and Se $4s$ orbitals, where the delay stabilizes. Figure 5 shows that the same is true for other photon energies. The underlying mechanisms that give rise to the Wigner delay structures will be discussed in the next section where we jointly examine Wigner delays and cross sections in terms of photon energies and polar emission angles.

C. Lowest-order mechanisms on small clusters

In this section we examine the mechanisms responsible for the cross section and time delay structures. Figures 7–12 present photoemission FDCSs and Wigner delays at $\phi = 0°$ and $\phi = 60°$, as functions of polar emission angle and photon

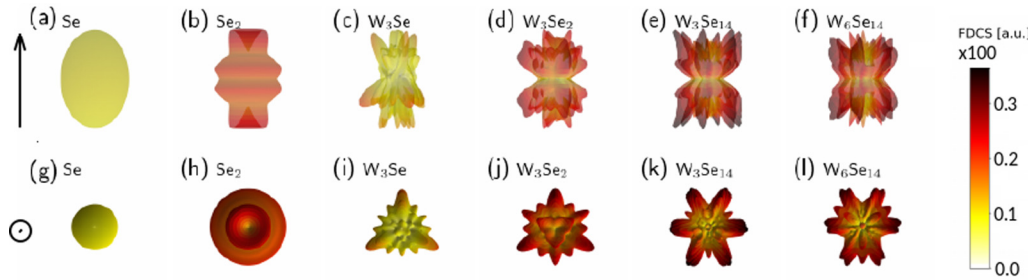

FIG. 3. Top row: Side view of the Se $3d$ photoemission FDCS at 91 eV photon energy, with light polarization along the z axis (indicated by the leftmost arrow and circle). Bottom row: top view of the Se $3d$ photoemission FDCS.

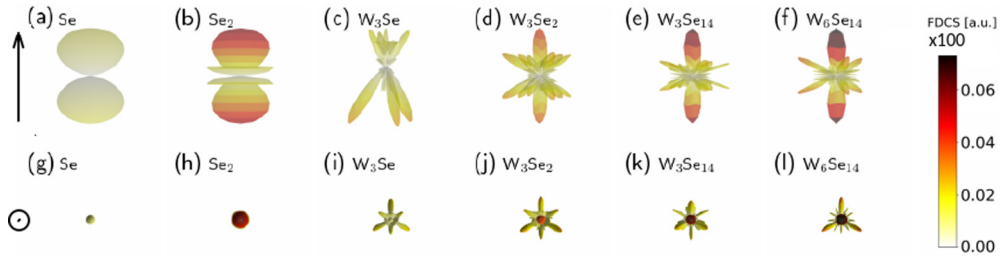

FIG. 4. Top row: Side view of the Se 4*s* photoemission FDCS at 91 eV photon energy, with light polarization along the z axis (indicated by the leftmost arrow and circle). Bottom row: top view of the Se 4*s* photoemission FDCS.

energy, in order to probe the effects of having or not having a neighboring atom in the emission plane. The specifics of scattering processes can be inferred by comparison, building up from smallest clusters to the more complex ones. We overlay the FDCS as contours over the Wigner time delays as a device to help us better distinguish the underlying processes.

The arguments in this section originate from three main points: (i) whether the cluster possesses one or two emitting atoms, (ii) scattering events, whether low angle scattering events (deflections) or sharp angle scattering effects (collisions or rebounds), and (iii) interference of two or more of the above. See Fig. 6 for a pictorial representation of these phenomena.

Before delving into the specific mechanisms present on each system, we have to point out that W 4f photoemission differs from Se 3d photoemission regarding point (i): while the central W atom is a single-atom emitter, the axial Se atoms make up a pair of emitters that can interfere with each other. If we analyze normal emission from any Se orbital, regardless of how the emission from the atom below is being scattered by the Se atom on top, the latter is always producing an unobstructed photocurrent.

In order to discuss the structures present in the FDCS and Wigner delays we will use the following naming convention. We start by the orbital in question, which in this work is one of 4s, 3d, or 4f, with no room for confusion regarding from which atomic species they originate. We denote the model cluster by a letter from A to F, as indicated by Table IV. The azimuthal emission angle ϕ is added next to the cluster identifier, and lastly, we add an integer counter for peaks belonging to a given orbital, cluster, and ϕ. By default we refer to peaks in the FDCS, and we preappend a "T" to the label if pointing to Wigner time delays.

TABLE III. Angularly integrated Wigner time delays $\langle\tilde{\tau}_{\mathrm{Wig},l}\rangle$ with an acceptance cone of 5° around the normal axis, in attoseconds, for the 91 eV experimental XUV photon energy in Ref. [10].

Orbital	W	WSe_3	WSe_6	W_7Se_6	W_7Se_{12}	W_7Se_{24}
W 4f	82	65	77	156	137	171
Orbital	**Se**	**Se_2**	**W_3Se**	**W_3Se_2**	**W_3Se_{14}**	**W_6Se_{14}**
Se 3d	71	88	120	103	185	198
Se 4s	15	48	29	70	95	100

We start with W 4f photoemission at $\phi = 0°$ in Fig. 7. We observe that the top Se layer addition to the isolated W introduces the most prominent feature in the FDCS, peak

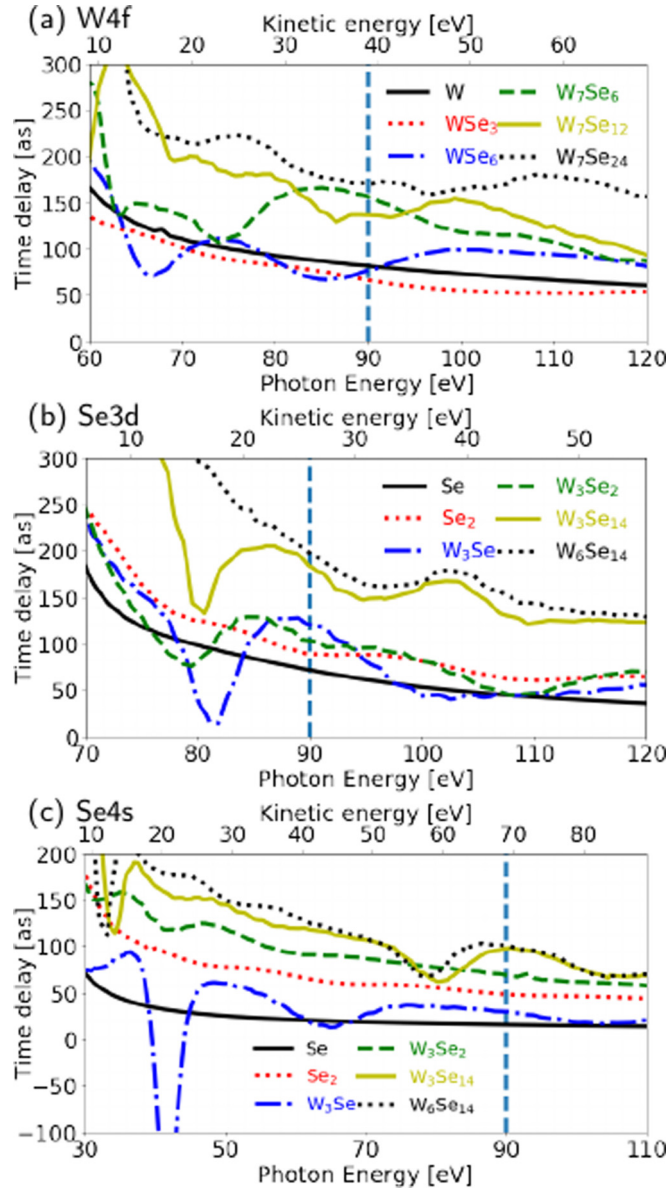

FIG. 5. Wigner time delays along the normal direction with a 5° acceptance cone. (a) W 4f, (b) Se 3d, and (c) Se 4s. The polarization direction is indicated by the leftmost arrow and circle.

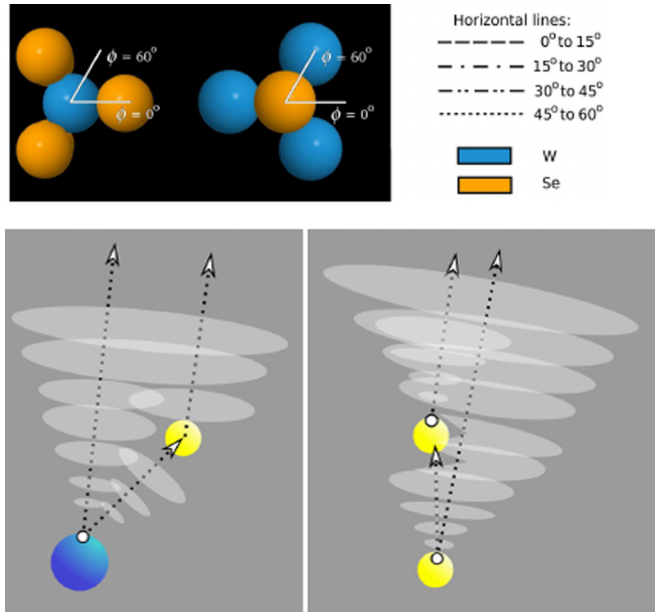

FIG. 6. Top panel: Azimuthal angle configurations and depiction of nearest neighbors in W-centric (left) and Se-centric clusters. To the right we present the line coding for the figures below, where we indicate the azimuthal distance to atoms lying at the given polar angle in said figures. Bottom panels: Pictorial representation of (a) a deflection and (b) two emitters leading to scattering plus interference.

4fB00|1. This is a constructive interference process with the scattered flux at the in-plane Se atom, marked by the yellow dashed line, right below the emission direction. The emission through the Se atoms, on the contrary, is inhibited. At near grazing emission there is another structure 4fB00|2 that stems from a similar process; however, for such emission polar angle our cluster model is not expected to match the periodic system, as in the latter case the electron would encounter other atoms. Both structures appear, albeit slightly reshaped, in panel (c): 4fC00|1 and 4fC00|2. Turning to $\phi = 60^\circ$, we note that no analogs to 4fB00|1 and 4fB00|2 are present in Fig. 8(b), meaning that it is a direct collision with the top Se atom, which takes place at $\phi = 0^\circ$ but not at $\phi = 60^\circ$, that gives rise to said structures.

An interesting picture emerges when comparing Figs. 7(b) and 8(b). There are no dominant features in Fig. 8(b), evidencing that the Se atoms lying away from the emission direction are only marginally affecting the electron flux. However, WSe_6 presents two peaks at $\phi = 60^\circ$, 4fC60|1 and 4fC60|2 [Fig. 8(c)], that manifest from a photoelectron probability rebound off the bottom Se layer, given that no similar structures

TABLE IV. Peak labeling scheme.

Label	A	B	C	D	E	F
W centric	W	WSe_3	WSe_6	W_7Se_6	W_7Se_{12}	W_7Se_{24}
Se centric	Se	Se_2	W_3Se	W_3Se_2	W_3Se_{14}	W_6Se_{14}

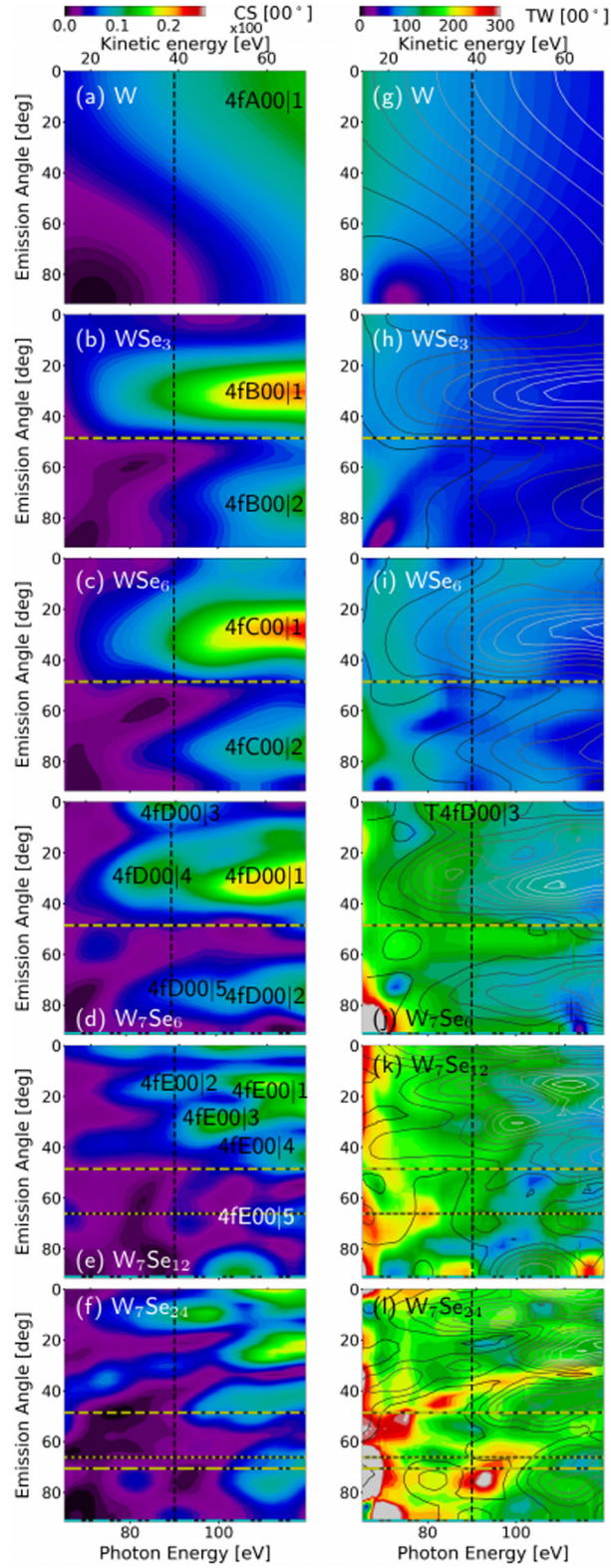

FIG. 7. FDCS and Wigner delays for W $4f$ photoemission from W, WSe_3, WSe_6, W_7Se_6, W_7Se_{12}, and W_7Se_{24} at $\phi = 0^\circ$. The CS and TW labels indicate FDCS and Wigner time delays, respectively. The number between brackets specifies ϕ for quick visual reference.

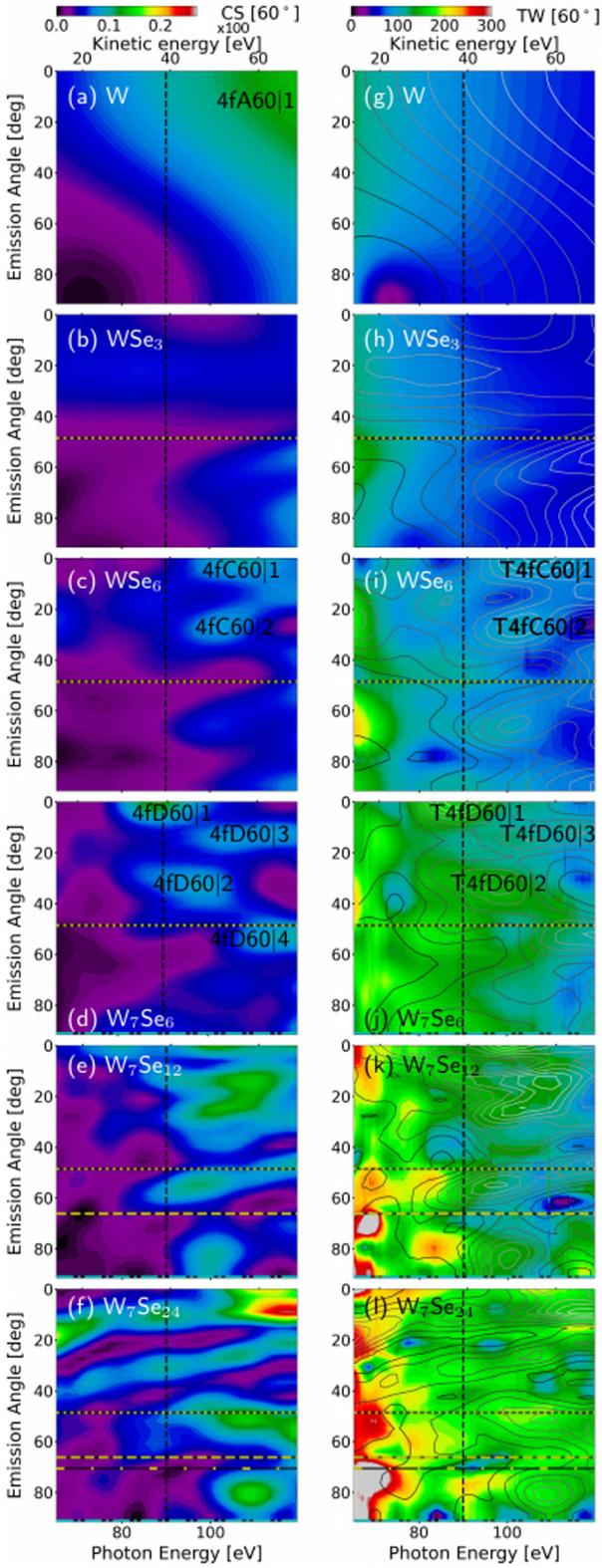

FIG. 8. FDCS and Wigner delays for W $4f$ photoemission from W, WSe_3, WSe_6, W_7Se_6, W_7Se_{12}, and W_7Se_{24} at $\phi = 60°$. The CS and TW labels indicate FDCS and Wigner time delays, respectively. The number between brackets specifies ϕ for quick visual reference.

are present in the WSe_3 case [Fig. 8(h)]. This off-Se rebound flux contributes some yield in the normal emission which is present for WSe_6 but not for WSe_3. Looking at the W, WSe_3, and WSe_6 time-delay structures supports the explanation, as the WSe_3 delay structure in both Figs. 7(h) and 8(h) closely resemble the isolated atom Wigner delays in Fig. 7(g). However, WSe_6 shows a more complex Wigner-delay structure. There are delay increases of 50–100 as corresponding to Wigner delay peaks T4fC60|1 and T4fC60|2. A careful comparison of peaks 4fB00|1 and 4fC00|1 shows that the latter has embedded structures analogous to 4fC60|1 and 4fC60|1, further supporting that they stem from flux rebounding off the bottom three Se atoms, as said structures are visible in Fig. 8(b) because there is no prominent low-angle deflection interference like 4fB00|1 along a ϕ missing a Se atom.

Noting that the addition of the six perimetric W atoms in W_7Se_6 introduces peaks 4fD00|3, 4fD00|4, and 4fD00|5 [Fig. 7(d)], none with an analog in smaller clusters, suggests therefore a direct participation of these W atoms. Peak 4fD00|3 is the same structure 4fD60|1 in Fig. 8(d), both lying at normal emission, and we see coincident Wigner delay increases T4fD00|1 and T4fD60|1, attesting to the travel time the photoelectron experiences inside the substrate. At $\phi = 60°$ we expect to see the interplay of many-center scattering, given that there is no Se atom lying in the emission plane that would otherwise yield the most dominant features.

The W_7Se_{12} cross section is very complex to disentangle extensively, but 4fE00|2, which lays at 20°, appears to be 4fD00|3 distorted in the same way 4fA00|1 becomes 4fB00|1 by a low-angle deflection against a Se atom in the emission plane. Four of the six W_7Se_{12} perimetral W atoms have a Se atom at their $\phi = 0°$, ending up with a 20° deflection of otherwise normally emitted (as would be the case for W_7Se_6) probability flux, for which only two W atoms have a Se neighbor to their right. Further backing the analogy is the fact that there is no significant change in delay between T4fD00|3 and the delay level (there is no peak) corresponding to 4fE00|2. Less prominent structures appear as analogs to 4fE00|2 in the $\phi = 60°$ case [Fig. 8(e)], which account for only three Se atoms lying in the plane of secondary emission at $\phi = 60°$ from the perimeter W atoms (see Fig. 1 for W_7Se_{12}). This supports the idea that photoelectron dynamics gains in complexity as we add more neighboring atoms in the pursuit of capturing its behavior inside the periodic system, considering that higher-order processes (i.e., beyond a single scattering event, appear in the larger model clusters. There is a practical limit to the ability to disentangle every mechanism involved: namely, the finite 4π solid angle. As more and more processes produce overlapping yield, the FDCS and Wigner-delay structures become inextricably entangled. The step-by-step cluster approach, however, allows us to explain the most prominent effects, and to an extent, determine how they get distorted and others are added when we study successively larger systems.

Some FDCS structures like 4fD60|1 to 4 all have a matching Wigner-delay increase, indicating that the processes correspond to time consuming scattering events with large

deflections, instead of minor ones (e.g., 4fB00|1). The distortion from 4fB00|1 and 2 to 4fC00|1 and 2, corresponding mostly to reflections on the bottom Se layer, do incur in Wigner-delay increases that are not present for WSe_3. However, the deflection and interference leading to the large FDCS structures 4fB00|1 and 2 do not seem to significantly delay the photoelectrons.

In Figs. 9 and 10 we turn to photoemission from the Se 3*d* orbital. The isolated-atom Se 3*d* emission is mostly isotropic, without strong angular dependencies within the energy ranges explored. The dimer exhibits four FDCS peaks, 3dB00|1 to 3dB00|4, that are produced by the dual emitters through mutual interference and scattering [see Fig. 6(b)]. These structures translate to the W_3Se_2 emission, which we will explain shortly. For Se-centric clusters, $\phi = 0^\circ$ means the outgoing photoelectron does not make an in-plane close-up to a W atom, which allows for the exploration of less prominent but more intricate collisions. In Fig. 9(c) the Se 3*d* photoemission FDCS from W_3Se evidences three peaks: 3dC00|1, 3dC00|2, and 3dC00|3 that originate from hard collisions with the W atoms [see Fig. 6(a)], given the Se atom is above the three W atoms, and the lowest order collision mechanism requires a downwards emission plus a sharp-angle scattering event with the W atoms below. It is worth noting that 3dB00|1 matches a 100 as Wigner-delay increase with respect to the isolated atom emission, supporting the interpretation of a rebound process being involved. The W_3Se_2 FDCS in Fig. 9(c) can be well described as a direct combination of the Se and W_3Se processes. There is a peak that appears in the W_3Se_2 FDCS, 3dD00|5, which does not have a clear parent on either Se_2's or W_3Se's FDCS. This leaves its interpretation to scattering events by the W atoms of the photocurrent emitted from the lower Se atom.

We turn to analyzing the $\phi = 60^\circ$ scenario (Fig. 10), where there is a W atom in the emission plane. The same type of low-angle collision type as seen in W 4*f* emission from WSe_3 is enabled from the bottom Se atom (W_3Se_2) as well as more direct in-plane photoelectron rebounds with a W atom [see Fig. 6(a)] for both W_3Se and W_3Se_2. The W_3Se system exhibits two notable peaks, labeled in Fig. 10(c) as 3dC60|1 and 3dC60|2. The latter, by comparison with isolated-Se emission, can be explained by a rebound process with the W layer, while the former corresponds to interference of direct emission [cf. Fig. 10(a), top right] and a rebound process. Having a W atom in the emission plane enables the detection of more direct collision processes that require lower momentum transfers than out-of-plane processes, and therefore, their amplitude is proportionally more significant. Peak 3dD60|4's origin is explained by looking at 3dC60|2, which implies a rebound process by the electron flux emitted by the top Se atom, although the reader can recall the same structure is observed for W_3Se_2 for $\phi = 0^\circ$ but not for W_3Se, leading to the interpretation that 3dD60|4 collects amplitude from two different processes: a reflection from the top photocurrent and a scattering process by the bottom one. The expected delay increases are similar, considering the path lengths are equivalently long, therefore the time-delay

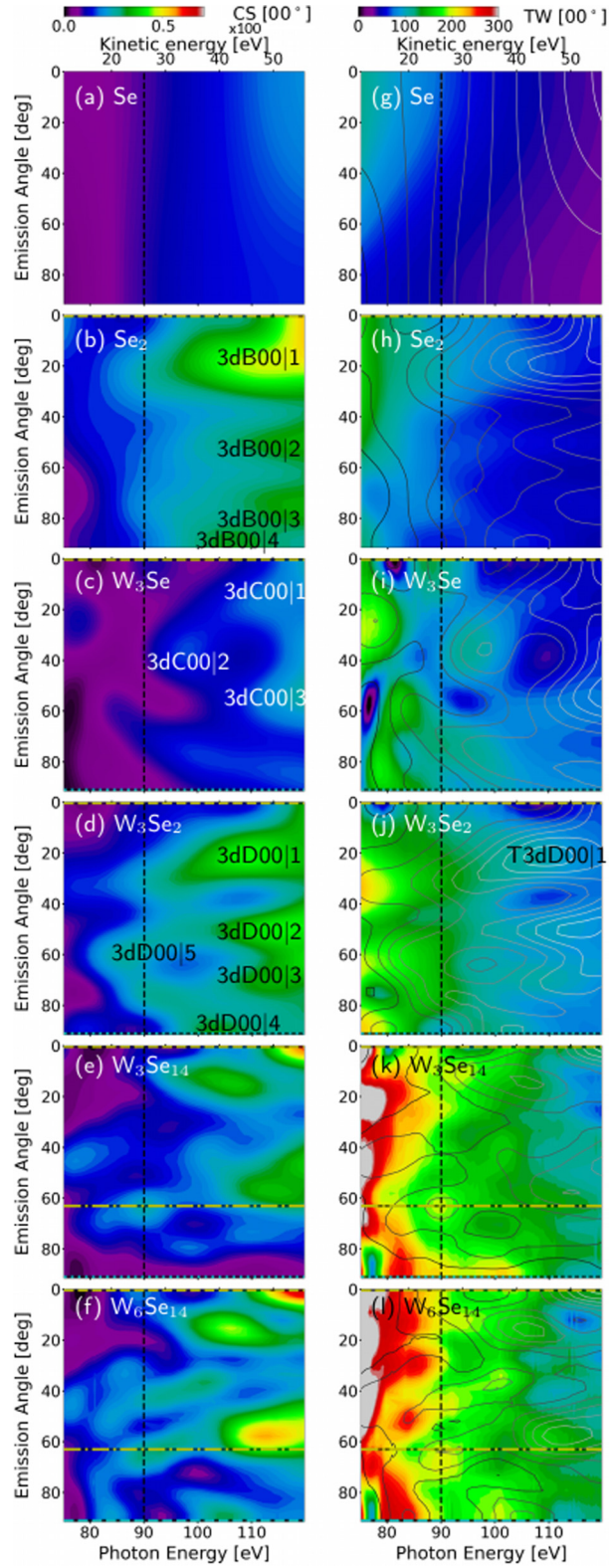

FIG. 9. FDCS and Wigner delays for Se 3*d* photoemission from Se, Se_2, W_3Se, W_3Se_2, W_3Se_{14}, and W_6Se_{14} at $\phi = 0^\circ$. The CS and TW labels indicate FDCS and Wigner time delays, respectively, and the number between brackets specifies ϕ for quick visual reference.

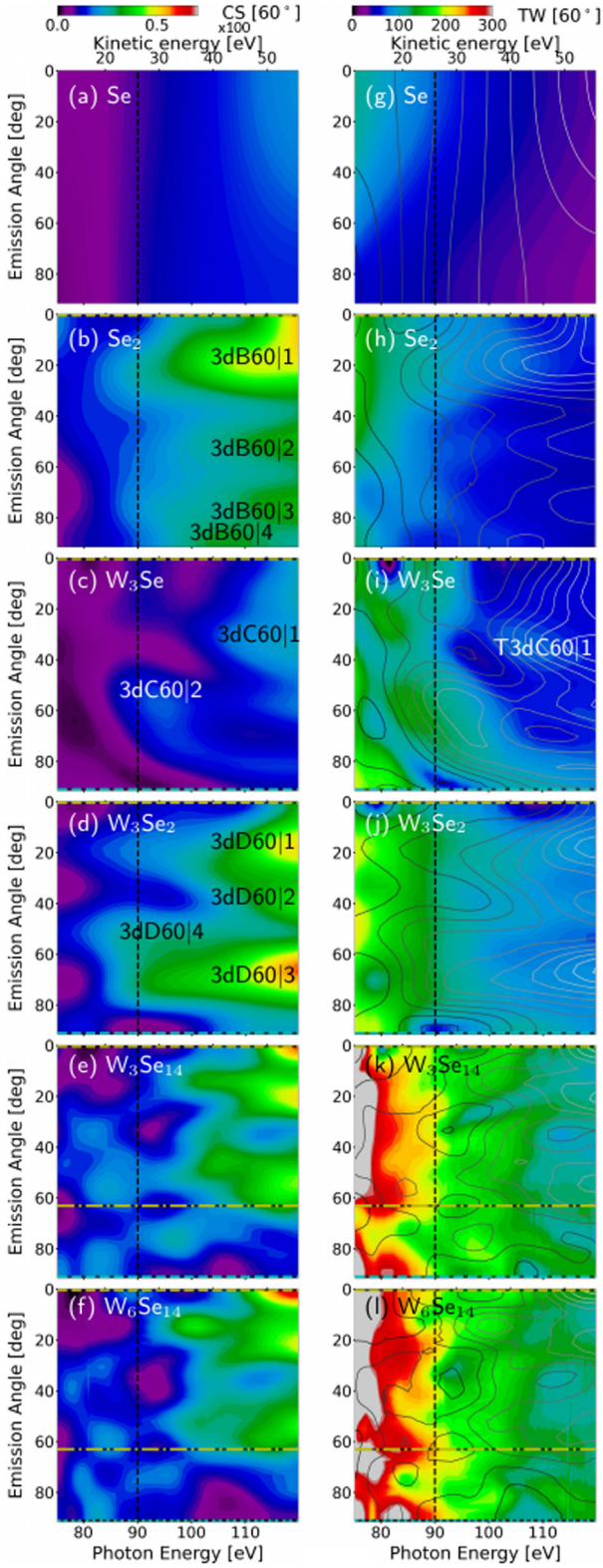

FIG. 10. FDCS and Wigner delays for Se 3*d* photoemission from Se, Se_2, W_3Se, W_3Se_2, W_3Se_{14}, and W_6Se_{14} at $\phi = 60°$. The CS and TW labels indicate FDCS and Wigner time delays, respectively, and the number between brackets specifies ϕ for quick visual reference.

structures do not add clarity to which of the two mechanisms is the more prevalent one. A comparison between 3dD00|3 and 3dD60|3 suggests there is a scattering mechanism enhancing the yield that adds to the emission pattern already present for Se_2 (peak 3dB60|3). Said scattering process corresponds to the emission from the bottom Se atom and its flux being scattered by the in-plane W atom, in a pattern analogous Fig. 6(a).

FDCS peaks 3dD00|1 [Fig. 9(d)] and 3dB00|1 appear to depend on the same process, namely, a constructive interference from the two scatterers just off normal emission, with some distortion introduced by reflective contributions from W atoms (cf. 3dC00|1). The presence of a second emitter for W_3Se_2 with respect to W_3Se, however, allows the flux coming from the bottom Se to scatter and then interfere with the otherwise unaffected yield. The time-delay increase T3dD00|1, which has no precursor on either Fig. 9(i) nor 9(h), suggests another higher-order contribution is taking place, which only affects the FDCS to a cosmetic degree.

At $\phi = 60°$, the structure named 3dD60|2 in Fig. 10 appears as a superposition of 3dB60|2 and 3dC60|1, and even at small clusters such as W_3Se_2 we run into the issue of having a finite solid angle to map the yield from many processes. All peaks 3dB60|1 to 4 do not correspond to sharp deflection processes, as there is no pronounced matching Wigner-delay increase. Instead, they are the product of constructive interference by the emission from both Se atoms. When examining W_3Se, we note the exact opposite happening at 3dC60|1, which does have an associated Wigner delay increase indicated at T3dC60|1. The picture is less evident for W_3Se_2, with the overall Wigner delay level being higher, indicating there are scatterng processes involved in W_3Se_2 that are absent with the simple dimer Se_2.

We now move on to Se 4*s* photoemission. Contrary to the previously studied initial orbitals, Se 4*s* produces a marked dipole pattern from the isolated atom, as shown in Fig. 11(a). The Se_2 dimer emission strongly inherits the overall dipole FDCS pattern and adds a strong constructive interference for normal emission [see Fig. 11(c), peaks 11(c)1 and 2].

We now proceed to dissect the visible structures. Figures 11(a) and 11(b) show how Se 4*s* photoemission FDCS changes between the Se isolated atom and the Se_2 dimer. Being an *s* state, the $l = 1$ pattern is discernible in the isolated-atom case, with a strong focus along the normal direction and a strict zero at 90°. The dimer FDCS is also heavily influenced by the dipole pattern; however, there are some interference effects leading to peaks 4sB00|1 and 2. Below these two main structures in Fig. 11(b) we see two fainter peaks, which have corresponding Wigner delays on par with the overall level for an isolated Se atom, suggesting there are no strong delaying effects like rebounds or confinement. Turning to W_3Se we see that at $\phi = 0°$ there are two salient structures 4sC00|1 and 2. These are coming from rebound processes, as we see there are matching time-delay increases. The W_3Se_2 picture at first glance resembles a direct composition of Se_2 and W_3Se structures; however, the peak 4sD00|4 seems to

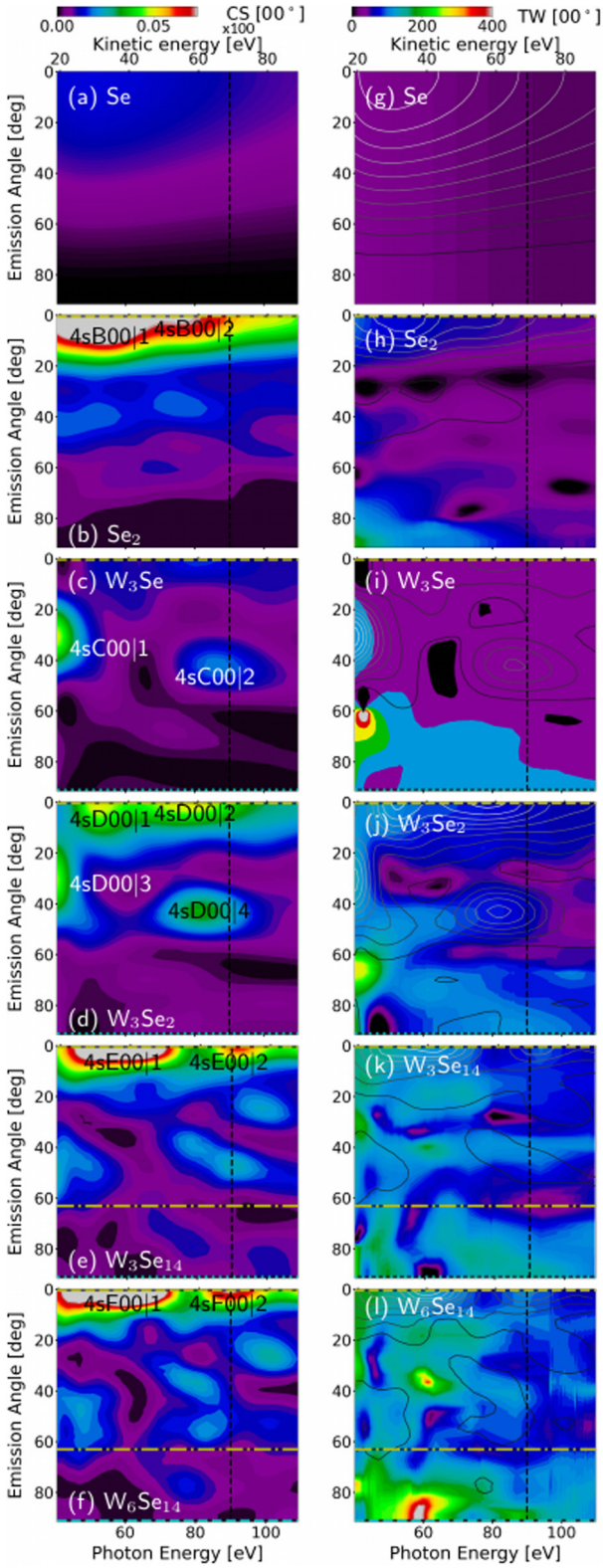

FIG. 11. FDCS and Wigner delays for Se 4*s* photoemission from Se, Se_2, W_3Se, W_3Se_2, W_3Se_{14}, and W_6Se_{14} at $\phi = 0°$. The CS and TW labels indicate FDCS and Wigner time delays, respectively, and the number between brackets specifies ϕ for quick visual reference.

be enhanced with respect to its predecessor W_3Se 4sC00|2, as well as slightly energy-shifted towards lower energies. This suggests an overlapping contribution from scattering events of the type shown in Fig. 6(a) off the two adjacent W atoms.

At $\phi = 60°$, W_3Se shows two FDCS peaks, 4sC601 and 2, which, not being present on the axially symmetric systems, and presenting corresponding Wigner-delay increases [Fig. 12(i)], we ascertain to be rebound processes with the W layer. The W_3Se_2 yield close to the normal direction, specifically peaks 4sD00|1 and 2, mimics the peaks inherited from the dimer peaks 4sB00|1 and 2, as well as adding the structures directly below them that translate from W_3Se 4sC60|1 and 2. Interestingly, 4sD60|4 is nearly identical to the $\phi = 0°$ peak 4sD00|4, suggesting that there is not a strong ϕ dependence to this structure, which in turn implies there may be a scattering contribution from all three W atoms in the middle layer. On the other hand, 4sD60|3 does not have an analog at $\phi = 0°$ emission, suggesting it stems from a deflection process with the in-plane W atom.

IV. CONVERGENCE WITH RESPECT TO CLUSTER SIZE

We now address the convergence of the FDCS and Wigner delays as we consider larger clusters. Starting with the W-centric clusters we note that, even between the largest clusters W_7Se_{12} and W_7Se_{24}, there are still significant changes (see the FDCS and time-delay plots in Figs. 7 and 8). The *sandwiched* nature of the W atom and a central emission pattern that is not a pure dipole extend the probability of a photoelectron encountering other neighbors and scattering.

The picture for the Se-centric systems seems to stabilize for the largest clusters in the present work. The Se 3*d* emission changes appreciably when switching from Se, to Se_2, to W_3Se, to W_3Se_2, and W_3Se_{14}. However, from W_3Se_{14} to W_6Se_{14} the structures appear to present lesser variation (see Figs. 9 and 10). A similar phenomenon is found for Se 4*s* (see Figs. 9 and 10), with W_3Se_2 already capturing many of the *final* features exhibited by the two largest Se-centric systems W_3Se_{14} and W_6Se_{14}. This is likely due to the pure dipole distribution from the emitting atoms, whereas for the Se 3*d* orbital, as we saw in Fig. 3, it is closer to isotropic, yielding probability current towards other neighbors. It is important to emphasize, however, that although we have not been able to reach full convergence of our FDCS with cluster size, the calculated Wigner delays for photoemission from Se atoms in the normal direction, both from the 3*d* and the 4*s* orbitals, for photoelectron energies > 20 eV (i.e., the case investigated in Ref. [10] and the most accessible one in current experiments), do not differ by more than 5% for the largest two clusters considered in this work as shown in Fig. 5. Therefore, we expect that, in this particular case, the values of the converged Wigner delays will not differ significantly from those reported in our paper.

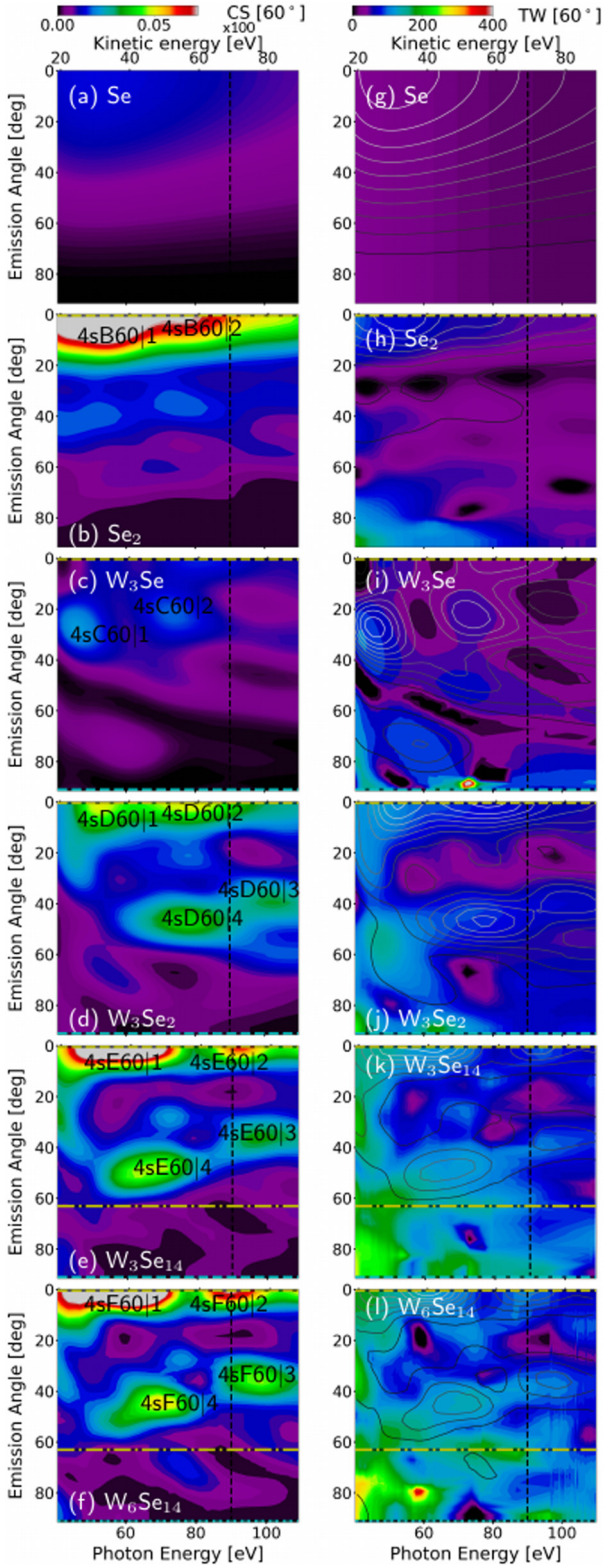

FIG. 12. FDCS and Wigner delays for Se 4*s* photoemission from Se, Se_2, W_3Se, W_3Se_2, W_3Se_{14}, and W_6Se_{14} at $\phi = 60°$. The CS and TW labels indicate FDCS and Wigner time delays, respectively, and the number between brackets specifies ϕ for quick visual reference.

V. SUMMARY

We have presented an in-depth analysis of the photoemission time delays and cross sections from the transition metal dichalcogenide WSe_2 for the specific orbitals W $4f$, Se $3d$, and Se $4s$, which are the experimental subjects of the work of Ref. [10]. We used a cluster approach to model the photoelectron emission dynamics while within a WSe_2 monolayer, fully accounting for the central atoms and their nearest neighbors, all of them described at the same level of accuracy. This has been achieved by means of the static-exchange DFT method, in which a symmetry-adapted partial wave expansion complemented by off-center few-partial-wave localized expansions centered at each atomic core [15] has been used. The use of *B*-spline basis functions for the radial coordinates ensures that, in this way, very fast oscillations of the continuum electron wave functions, can be accurately described.

We observe a strong influence of neighboring atoms on both the Wigner delays and differential cross sections. We have been able to distinguish the underlying mechanics by comparing different model clusters, two azimuthal emission angles, while spanning through the emission energy and polar angle. Our step-by-step approach has allowed us to disentangle some of the low-order processes that take place, which would not have been accessible by aiming only at the largest computationally tractable clusters.

It is also important to emphasize that this study would not have been possible by using many-body methodologies as those available to study photoionization of atoms and molecules in the gas phase. These methodologies provide in principle a more accurate description of electron correlation than our static-exchange DFT method. But they are computationally much more demanding and, therefore, they are only applicable to very small clusters containing W and Se atoms. Although the static-exchange DFT method approximately incorporates electron correlation through the exchange-correlation functional and this level of description has been shown to be good enough to describe photoionization of atoms and molecules in the gas phase at not too-low energies, one cannot totally rule out that a more sophisticated treatment of electron correlation might be necessary to describe the interaction of the escaping photoelectron with those electrons lying in very delocalized bands. However, existing work on transition metal dicalchogenides (see, e.g., Ref. [7], and references therein), shows that a DFT-KS approach, though not able to catch the tiniest details of the electronic structure of these materials, is able to describe the most important qualitative features. Therefore, one can reasonably expect that our predictions will remain valid, at least qualitatively, even when higher-level many-body methods become accessible in the future.

A similar approach is expected to shed light on the role played by the IR pulse that accompanies XUV-induced ionization in any streaking measurements, which are currently performed to provide quantitative information about photoemission delays in condensed-matter systems. For this, a time-dependent implementation of the present approach

would be necessary. Work along this line is currently in progress in our group.

ACKNOWLEDGMENTS

This work has been supported in part by the Basque Departamento de Educación, Universidades e Investigación, the University of the Basque Country UPV/EHU (Grant No. IT1246-19) and the Spanish Ministerio de Ciencia e Innovación projects PID2019-107396GB-I00 and PID2019-105458RB-I00, the "Severo Ochoa" Programme for Centres of Excellence in R&D (SEV-2016-0686), and the "María de Maeztu" Programme for Units of Excellence in R&D (CEX2018-000805-M). We acknowledge the computation time awarded to this research on MareNostrum 4 cluster, QS-2021-1-0037, QS-2020-3-0036, FI-2020-2-0007, FI-2020-1-0009, and the Centro de Computación Científica (CCC) of Universidad Autónoma de Madrid.

[1] Q. Cheng, J. Pang, D. Sun, J. Wang, S. Zhang, F. Liu, Y. Chen, R. Yang, N. Liang, X. Lu, Y. Ji, J. Wang, C. Zhang, Y. Sang, H. Liu, and W. Zhou, InfoMat **2**, 656 (2020).

[2] D. Voß, P. Krüger, A. Mazur, and J. Pollmann, Phys. Rev. B **60**, 14311 (1999).

[3] U. Krishnan, M. Kaur, K. Singh, M. Kumar, and A. Kumar, Superlattices Microstruct. **128**, 274 (2019).

[4] H. Tian, M. L. Chin, S. Najmaei, Q. Guo, F. Xia, H. Wang, and M. Dubey, Nano Res. **9**, 1543 (2016).

[5] J. Liu, H. Liu, J. Wang, H. Sheng, G. Tang, J. Zhang, and D. Bai, Phys. B: Condens. Matter **568**, 18 (2019).

[6] Q. Feng, H. Deng, H. Yang, S. Ke, H. Lv, L. Li, and X. Zu, Results Phys. **28**, 104605 (2021).

[7] M. Pisarra, C. Díaz, and F. Martín, Phys. Rev. B **103**, 195416 (2021).

[8] I. Tanabe, T. Komesu, D. Le, T. B. Rawal, E. F. Schwier, M. Zheng, Y. Kojima, H. Iwasawa, K. Shimada, T. S. Rahman, and P. A. Dowben, J. Phys.: Condens. Matter. **28**, 345503 (2016).

[9] R.-Y. Liu, Y. Ogawa, P. Chen, K. Ozawa, T. Suzuki, M. Okada, T. Someya, Y. Ishida, K. Okazaki, S. Shin, T.-C. Chiang, and I. Matsuda, Sci. Rep. **7**, 15981 (2017).

[10] F. Siek, S. Neb, P. Bartz, M. Hensen, C. Strüber, S. Fiechter, M. Torrent-Sucarrat, V. M. Silkin, E. E. Krasovskii, N. M. Kabachnik, S. Fritzsche, R. D. Muiño, P. M. Echenique, A. K. Kazansky, N. Müller, W. Pfeiffer, and U. Heinzmann, Science **357**, 1274 (2017).

[11] E. Saydanzad, J. Li, and U. Thumm, Phys. Rev. A **98**, 063422 (2018).

[12] F. Süßmann and M. F. Kling, Phys. Rev. B **84**, 121406(R) (2011).

[13] M. Venuti, M. Stener, and P. Decleva, Chem. Phys. **234**, 95 (1998).

[14] M. Stener, G. Fronzoni, D. Toffoli, and P. Decleva, Chem. Phys. **282**, 337 (2002).

[15] D. Toffoli, M. Stener, G. Fronzoni, and P. Decleva, Chem. Phys. **276**, 25 (2002).

[16] D. Toffoli and P. Decleva, J. Chem. Theory Comput. **12**, 4996 (2016).

[17] E. Plésiat, M. Lara-Astiaso, P. Decleva, A. Palacios, and F. Martín, Chem. A: Eur. J. **24**, 12061 (2018).

[18] R. van Leeuwen and E. J. Baerends, Phys. Rev. A **49**, 2421 (1994).

[19] G. te Velde, F. M. Bickelhaupt, E. J. Baerends, C. Fonseca Guerra, S. J. A. van Gisbergen, J. G. Snijders, and T. Ziegler, J. Comput. Chem. **22**, 931 (2001).

[20] E. v. Lenthe, E. J. Baerends, and J. G. Snijders, J. Chem. Phys. **99**, 4597 (1993).

[21] E. van Lenthe, E. J. Baerends, and J. G. Snijders, J. Chem. Phys. **101**, 9783 (1994).

[22] E. van Lenthe, A. Ehlers, and E.-J. Baerends, J. Chem. Phys. **110**, 8943 (1999).

[23] H. Bachau, E. Cormier, P. Decleva, J. E. Hansen, and F. Martín, Rep. Prog. Phys. **64**, 1815 (2001).

[24] C. W. McCurdy, T. N. Rescigno, C. S. Trevisan, R. R. Lucchese, B. Gaire, A. Menssen, M. S. Schöffler, A. Gatton, J. Neff, P. M. Stammer, J. Rist, S. Eckart, B. Berry, T. Severt, J. Sartor, A. Moradmand, T. Jahnke, A. L. Landers, J. B. Williams, I. Ben-Itzhak *et al.*, Phys. Rev. A **95**, 011401(R) (2017).

[25] E. P. Wigner, Phys. Rev. **98**, 145 (1955).

[26] R. Pazourek, S. Nagele, and J. Burgdörfer, Rev. Mod. Phys. **87**, 765 (2015).

[27] N. E. Hurt, in *Quantum Chaos and Mesoscopic Systems: Mathematical Methods in the Quantum Signatures of Chaos* (Springer Netherlands, Dordrecht, 1997), pp. 179–196.

[28] C. Texier, Phys. E (Amsterdam, Neth.) **82**, 16 (2016).

[29] D. Baykusheva and H. J. Wörner, J. Chem. Phys. **146**, 124306 (2017).

[30] M. Ossiander, F. Siegrist, V. Shirvanyan, R. Pazourek, A. Sommer, T. Latka, A. Guggenmos, S. Nagele, J. Feist, J. Burgdörfer, R. Kienberger, and M. Schultze, Nat. Phys. **13**, 280 (2017).